This manuscript has been accepted in Chemical Geology on the 2nd November 2020 after a peer-review process

Apatite fission-track dating by LA-Q-ICP-MS imaging

Claire Ansberque[1]*, David M. Chew[1], Kerstin Drost[1]

Department of Geology, School of Natural Sciences, Trinity College Dublin,College Green, Dublin 2, Ireland

*corresponding author: ansberqc@tcd.ie

Abstract

Obtaining accurate and precise apatite fission-track (AFT) ages depends on the availability of high-quality apatite grains from a sample, ideally with high spontaneous fission-track densities (c. >1.10^5 tracks.cm^{-2}). However, many natural samples, such as bedrock samples from young orogenic belts or low-grade metamorphic samples with low U contents yield low spontaneous fission-track densities. Such apatites must be counted to avoid biasing the resultant FT age. AFT dating employing LA-Q-ICP-MS spot ablation works very well for grains with high spontaneous fission-track densities. This approach allows detection of potential U zoning, while also removing the need for an irradiation step and facilitating simultaneous acquisition of U-Pb and trace element data. The LA-Q-ICP-MS spot ablation thus offers several advantages compared to the External Detector Method (EDM). However, the spot ablation approach requires the counted area to mimic exactly the site and size of the laser spot, which for grains with low spontaneous fission-track densities (<10^5 tracks.cm^{-2}), implies fewer track counts and impairs the precision of the resultant AFT age. Here we present an alternative approach to LA-Q-ICP-MS spot analysis of low fission-tracks density grains by generating a U distribution ($^{238}U/^{43}Ca$) map of the entire apatite surface by LA-Q-ICP-MS elemental mapping, which enables characterization of U zonation. The Monocle plugin for the Iolite LA-ICP-MS data reduction software is used to display elemental maps and extract mean $^{238}U/^{43}Ca$ values of the same area counted for the fission-tracks. A typical grain-mapping session takes < 5 hours to map 80 grains. The method was employed on the Durango and Fish Canyon Tuff apatite reference materials, six bedrock apatite samples with low fission-track densities (≤ 1.10^5 track.cm^{-2}), and one bedrock apatite sample with high fission-track density (>1.10^6 track.cm^{-2}) to assess the precision and accuracy of our approach. Most apatite samples investigated here were previously dated by the

EDM or the LA-Q-ICP-MS ablation spot method. The AFT grain-mapping ages agree with previously published EDM or LA-Q-ICP-MS spot ablation ages at the 2σ level. For each apatite sample, we simultaneously acquired U-Pb age and trace element data (Mn, Sr, La, Ce, Sm, Eu, Gd, Lu); here again the data agree with literature constraints (when available) within uncertainties. The mapping approach is therefore a practical solution to low-temperature thermochronology studies facing apatite grains with low spontaneous fission-track densities, while also facilitating investigation of the spatial relationships between thermo- and geochronometric ages and grain chemistry.

Keywords: Elemental mapping; AFT and U-Pb dating; rare earth elements; Durango; Fish Canyon Tuff; Cyclades; Western Himalaya; Scotland

1. Introduction

Apatite fission-track (AFT) thermochronology is a well-established method for investigating the thermal history of the crust within a near surface to 120˚C temperature window (Green et al., 1986; Wagner and Van den Haute, 1992; Spiegel et al., 2007; Tamer and Ketcham, 2020). The method is widely employed to constrain mountain range development through time, reconstruct the thermal history of sedimentary basins, or determine the provenance of clastic sediments (see Malusà and Fitzgerald, 2019 for a review of AFT applications). However, AFT is a time-consuming dating method since spontaneous fission-tracks, corresponding to the natural fission of ^{238}U in apatite, must be counted (or verified in the case of automatically counted fission-tracks) by a human operator. AFT age determination also requires measuring the parent U distribution in the dated apatite crystal. This has traditionally been determined using the external detector method (EDM), which involves inducing fission-tracks in a U-free muscovite attached to the apatite grain surface, by irradiation with thermal neutrons in a nuclear reactor, etching the muscovite, and counting the induced fission-tracks on the latter (see Hurford and Green, 1982; Wagner and Van den Haute, 1992, Gallagher et al., 1998, and Tagami and O'Sullivan, 2005, for a description of the EDM). The EDM protocol is therefore time consuming due to the irradiation, post-irradiation cooling period and counting of both spontaneous and induced fission-tracks. LA-Q-ICP-MS (laser ablation quadrupole inductively-coupled-plasma mass spectrometer) spot analysis has been successfully employed in AFT dating for the *in-situ* measurement of apatite $^{238}U/^{43}Ca$ ratio (e.g., Hasebe et al., 2004; 2013; Chew and Donelick, 2012; Vermeesch, 2017; Cogné et al., 2020). This approach is rapid as it avoids the need for irradiation and counting of induced fission-tracks, limits the use of hazardous acids, and can also yield additional information such as apatite Cl contents (Chew et al., 2014a), apatite U-Pb age data (e.g. Chew et al., 2014b) and apatite trace element information which can be exploited to yield host rock-type information (e.g., Dill 1994; Sha and Chappell, 1999; Belousova et al., 2002; O'Sullivan et al., 2020).

The main advantage of the EDM approach is that identical areas are counted on individual apatite grains and their mirror images in the muscovite detector. Therefore, the distribution of induced fission-tracks in the muscovite detector is a reliable proxy map for the U distribution in the apatite grain and for detecting U-zonation if present. This induced fission-track map also records depth-integrated variations in U concentration, as induced fission (like spontaneous fission) generates tracks in the muscovite detector up to half a fission-track length below the apatite grain surface. However, U zonation can typically only be detected when the spontaneous fission-track density is > c. 1.10^5 tracks.cm^{-2}. With the LA-Q-ICP-MS spot analysis approach, if the dated apatite has a homogeneous fission-track distribution over its entire surface (i.e. no U zonation), the size and location of the counted area and that of the ablation spot (typically c. 30 µm in diameter) can be matched without impairing the precision of the resultant AFT age. However, if the spontaneous fission-track density is < c. 1.10^5 tracks.cm^{-2} (i.e. samples with low U and/or yielding young AFT ages), matching the size of the counted area to that of the ablation spot results in fewer spontaneous fission-track counts and thus less precise single-grain AFT ages (Vermeesch, 2017).

An alternative to laser ablation spot analysis to detect potential U zonation in grains with low spontaneous fission-track density is to generate a two-dimensional U distribution map over the entire grain surface by LA-Q-ICP-MS mapping. This technique combines the advantages of the EDM (detection of U zonation in young and/or with low U apatite) with those of the LA-Q-ICP-MS (rapidity, and simultaneous acquisition of U-Pb and trace element data). Here we present such an elemental mapping approach by LA-Q-ICP-MS to AFT dating employing a fast-washout laser cell with an aerosol rapid introduction system (ARIS, van Malderen et al., 2018) which allows for rapid and precise characterisation of elemental distributions on the entire grain surface (Petrus et al., 2017; Ubide et al., 2015; Chew et al., 2019). Our approach assumes that the observed U-concentration on the grain surface is constant at depth. This assumption is reasonable as in our approach, the top c. 3 µm of the grain surface is analysed. Uranium within 3 µm of the apatite grain surface generates over 50% of the spontaneous tracks, while any potential µm-scale U zoning with depth would have to be non-systematic to affect age accuracy. If µm-scale variations in U zoning with depth were randomly distributed, then the age accuracy of individual grains would decrease but the central and pooled ages would remain the same but with more dispersion. Following data reduction with the Iolite software (Paton et al., 2011), mean elemental abundances and mean elemental and isotopic ratios are extracted from user-defined areas on the apatite grain maps (which are similar to the fission-track counted area) using the 'Monocle' map interrogation tool for Iolite (Petrus et al., 2017). This grain-mapping approach for AFT dating presented here is easily implemented by any laboratory with an LA-Q-ICP-MS system and we provide details from sample preparation through to the data acquisition protocol, along with recommendations for future research using the approach.

2. Sample information and preparation protocols

2.1 Samples used in this study

We tested the grain-mapping approach for AFT dating on Durango and Fish Canyon Tuff apatites, which are well-characterised in terms of both AFT and U-Pb ages and which we treated as unknowns to assess the reproducibility of the technique (termed "Dur_unk" and "FCT_unk", respectively). We also analysed six bedrock samples from Henrichs et al. (2018), Vannay et al. (2004) and Treloar et al. (2000), all of which come from rapidly exhumed terranes and were previously analysed for AFT and/or U-Pb dating. These bedrock samples were selected because of their young AFT ages and their variable U contents (between c. 1 and 300 ppm). To evaluate the precision of our approach we also analysed an apatite bedrock sample with known old AFT age, high fission-track density (>1.10^{6} tracks.cm^{-2}) and known U zonation. Hereafter adopted AFT ages obtained with the EDM or LA-Q-ICP-MS spot ablation techniques are noted AFT_{EDM} or AFT_{spot}, respectively.

The Durango fluorapatite sample is a crushed fragment of a single large crystal from the iron oxide deposit at Cerro de Mercado, Mexico. The deposit is bracketed by two major ignimbrites from which sanidine-anorthoclase yielded $^{40}Ar/^{39}Ar$ age of 31.44 ± 0.18 Ma (2σ level; McDowell et al., 2005). Apatite FT_{spot} and U-Pb dating of Durango fluorapatite has yielded ages of 30.6 ± 5.4 Ma (2σ level; Hasebe et al., 2004) and 30.87 ± 0.82 Ma (2σ level; Thompson et al., 2016), respectively. Chew et al. (2016) acquired trace element data by solution ICP-MS on aliquots of the same crushed Durango fluorapatite as analysed in this study and these data are presented along with our results in Section 4.3.

Fish Canyon Tuff fluorapatite comes from a vast phenocryst-rich dacite with a rhyolitic matrix in the San Juan Volcanic Field of southern Colorado, from which sanidine phenocrysts have yielded an $^{40}Ar/^{39}Ar$ age of 28.13 ± 0.02 Ma (2σ level; Phillips et al., 2017). Apatite FT_{spot} and U-Pb dating of Fish Canyon Tuff fluorapatite has yielded ages of 29.7 ± 3.8 Ma (2σ level; Hasebe et al., 2004), and

29.1 ± 0.7 Ma (2σ level; Chew et al., 2014b), respectively. Pang et al. (2017) have acquired trace element data (excluding Th, U, Sr) by LA-ICP-MS on Fish Canyon Tuff apatite (see Section 4.3).

RM13 is an upper amphibolite-facies paragneiss sample collected from the central part of the migmatite dome on Paros Island (Greek Cycladic Islands), which yielded a U-Pb age of 11.5 ± 3.8 Ma (95% conf.; model 1 regression; Henrichs et al., 2018). These authors also documented the apatite trace element abundances in sample RM13 (see Section 4.3). There are presently no published AFT ages for sample RM13, but three samples collected from the same unit a few kilometres to the west yielded AFT_{EDM} central ages ranging from 10.5 ± 2.0 to 12.5 ± 2.8 Ma (2σ level; Brichau et al., 2006).

Apatite samples hb3197 and hb4396 from Vannay et al. (2004) were collected from the Wangtu Gneiss Complex (from the Jutogh Group of the Lesser Himalayan Crystalline Sequence), which yielded a U-Pb zircon crystallization age of c. 1.8 Ga (Chambers et al., 2008; Kohn et al., 2010). Although there are no U-Pb age constraints for samples hb3197 and hb4396, monazite from a pelitic schist (Caddick et al., 2007) and uraninite from a leucogranite (Chambers et al., 2008), both from the Jutogh Group, yielded U-Pb ages of 10.6 ± 0.9 and 10.5 ± 1.1 Ma respectively, which dates the latest tectono-thermal event in the Lesser Himalayan Crystalline Sequence (upper amphibolite facies, ca. 640-700˚C; Vannay et al., 2004; Caddick et al., 2007). Samples hb3197 and hb4396 yielded young AFT_{EDM} central ages of 0.7 ± 1.2 Ma, and 1.7 ± 1.0 Ma respectively (2σ level; Vannay et al., 2004). There are no trace element data available for these two apatite samples in the literature.

Apatite samples him610/205, him618/230 and him622/244 from Treloar et al. (2000) were collected along the Astor River in the Shengus Gneiss of the Nanga Parbat massif (Pakistan). Samples him610/205, him618/230 and him622/244 yielded AFT_{EDM} central ages of 1.7 ± 0.2 Ma, 0.4 ± 0.2 Ma, and 0.03 ± 0.04 Ma (considered as a 0 Ma AFT age) respectively (2σ level; Treloar et al., 2000). There are presently no U-Pb ages for those three apatite samples, however Treloar et al. (2000) obtained a hornblende Ar/Ar age of 27 ± 1 Ma on sample him610/205 and documented a cooling event through 500 ˚C at 25 ± 5 Ma along the Astor River. Ar-Ar biotite cooling ages ≤ 5 Ma are also present in the Nanga Parbat massif (e.g., Zeitler et al., 2001). There are no trace element data available for these three apatite samples in the literature.

Finally, the apatite sample RC2168 (Sct-8) from Döpke (2017) was collected from a felsic intrusion in the eastern Grampian Terrane of Scotland. This apatite sample yielded central and pooled AFT ages of 316 ± 38 Ma and 309 ± 26, respectively, and a U-Pb age of 484 ± 21 Ma (2σ level, Döpke, 2017). There are no trace element data available for this sample in the literature.

2.2 Sample preparation

All samples were pure apatite separates that were processed at the Fission-Track Laboratory at the Geology Department, Trinity College Dublin. Each apatite sample was mounted on 15 mm diameter, 2 mm thin epoxy resin discs (Fig. 1a), which was then grounded for 20 s and polished for several minutes with a LaboPol-21 Struers® polisher (equipped with a LaboForce-3 and LaboDoser) and Struers® diamond-based suspensions (from 6 to 1 μm) to expose internal apatite surfaces. Apatite mounts were etched in 5.5M HNO3 at 21 ± 0.5 ˚C for 20 ± 1 s to reveal spontaneous fission-tracks (Donelick et al.,1999), and then rinsed thoroughly in deionised water.

Three copper target grids of 3.05 mm diameter (Agar scientific) were affixed to each mount using a water-based glue to enable coordination of the grains (Fig. 1a). Spontaneous tracks were then counted over the entire surface (excluding the outer 10 μm crystal rim; Donelick et al., 2005) of c-axis parallel apatites at x1000 magnification using a Zeiss Axiom Z1m microscope equipped with a camera and the TrackWorks software (Autoscan Systems). The TrackWorks software also permits coordination of the grain centres relative to the target grid positions, delimiting the counted area on each grain and measurement of the etch-pit length (D_{par}). To obtain well constrained ages, we selected from 40 to 70 grains per sample. Fewer grains were counted for the Durango, Fish Canyon Tuff and RC2168 apatite samples (n= 26, 29, 36, respectively). The grain sizes were typically > 120 μm x 100 μm, and the approach was tested on grains as small as c. 95 μm x 55 μm.

The datafile exported by TrackWorks includes for each grain the sum of the counted spontaneous fission-tracks (N_s), the fission-track density (ρ_s), and the grain X-Y coordinates. The grain coordinates are imported into the laser ablation software (Chromium 2.3, Teledyne CETAC Technologies) to facilitate rapid relocation of the grains for subsequent elemental mapping. Prior to LA-Q-ICP-MS data acquisition, apatite mounts were cleaned in alcohol and deionised water in an ultrasonic bath for 10 minutes to remove any surficial common Pb (Pb_c) contamination to not prejudice U-Pb age measurements.

In this study, we followed the zeta-based approach for AFT dating described by Cogné et al. (2020; see Section 3.4.1). This approach involves (i) FT counting of c-axis parallel, c. 300 μm-long Durango apatite shards on a “zeta” mount (called “Dur_zeta”), (ii) determination of the U/Ca ratio of the Durango shards over one long primary LA-Q-ICP-MS zeta session where grains are ablated three times each, and (iii) calculation of a zeta factor. These Durango shards are then reanalysed during all LA-Q-ICP-MS sessions. While typically up to 20 spot ablations can be placed on each Durango zeta shard, the mapping approach to AFT dating employs much larger areas and hence uses up the pool of FT-counted zeta shards more quickly. It is feasible to reanalyse over a previously ablated surface during subsequent grain mapping sessions (which was undertaken twice during this study), or to re-polish the “Dur_zeta” mount between the sessions (which was undertaken five times in total in this study removing a total depth of c. 15 μm on each “Dur_zeta” shard). Hence, for the “Dur_zeta” mount the copper target grids were replaced by three distinct reference marks each comprising two large ablation patterns for location purposes adjacent to a smaller pattern of the same shape. The latter was used for the fine-scale referencing (Fig. 1a); these ablation patterns are sufficiently deep (> 50 μm) to survive multiple re-polishing steps.

3. Method

3.1 Data Acquisition

We performed all LA-Q-ICP-MS mapping sessions at the Centre for Microscopy and Analysis at Trinity College Dublin using a Teledyne Photon Machines Analyte Excite 193 nm ArF excimer laser system with a two-volume ablation cell (Müller et al., 2008; van Malderen et al., 2016) coupled to an Agilent 7900 Q-ICP-MS. The aerosol was transported from the laser cell to the mass spectrometer using an aerosol rapid introduction system (ARIS; van Malderen et al., 2018) with short polyetheretherketone (PEEK) tubing and subsequently mixed in a volume-variable smoothing device with Ar carrier gas and N_2 to enhance signal sensitivity and reduce oxide formation.

Laser and Q-ICP-MS operating conditions are summarised in Table 1 and were optimised to satisfy the following criteria: producing a sufficient volume of aerosol during the ablation process (with the main determining factor being optimal acquisition of the full isotope suite required for U-Pb analysis), allocating sufficient mass sweep times per ablation line to produce high-resolution maps that resolve elemental zonation on a typical 100 µm-wide apatite grain, and rapidly acquiring data with limited carry over from zones of varying U concentration or from one ablation line scan (raster line) to another. Operating conditions were optimised daily by LA-Q-ICP-MS tuning on NIST 612 SRM silicate glass to yield (i) maximum sensitivity for ^{238}U while maintaining a Th/U ratio close to unity and (ii) low production rates of oxides and doubly charged ions which were monitored by analysis of ThO^+/Th^+ and Ca^{2+}/Ca^+ respectively (Table 1). Once optimised, the same LA-Q-ICP-MS parameters were applied to both standards and unknowns and across all experiments. The ablation pit depth on the grain surface during a raster line was determined using a Filmetrics white light interferometer and is c. 3 µm-deep (Fig. 1b).

All data were acquired as time-resolved signals derived from a series of horizontal and adjacent parallel raster lines, which populate a user-defined rectangular area defined within the Chromium 2.3 software. For the unknowns, the user-defined area systematically covers the entire grain surface and partly the surrounding epoxy resin (Fig. 1a). Data on primary standards (see the Data Reduction Section 3.2) were acquired from three to four parallel raster lines without overlapping the epoxy resin and for a minimum duration per raster of c. 25 s. We allowed a 10 s background acquisition (washout) between each raster line for both standards and unknowns (Fig. 1a).

A sample-standard bracketing approach is systematically employed to correct for ICP-MS sensitivity drift, which involves intercalating c. 5 to 10 unknowns (corresponding to between c. 45 to 75 raster lines) in between a series of reference materials. These include NIST 612 SRM silicate glass, Durango apatite (fifteen shards of the “Dur_zeta” mount) and the U-Pb standards Madagascar apatite and McClure Mountain apatite (Chew et al., 2014b).

For all mapping sessions (seven sessions in total for nine analysed samples), the ICP-MS monitored fourteen masses, which were selected for AFT dating (^{238}U, ^{43}Ca), U-Pb ages (^{238}U, ^{232}Th, $^{206, 207, 208}Pb$), and key trace and rare earth element abundances which have petrogenetic significance in apatite (^{55}Mn, ^{88}Sr, ^{139}La, ^{140}Ce, ^{147}Sm, ^{153}Eu, ^{157}Gd, ^{175}Lu; e.g., O’Sullivan et al., 2020). We allocated a dwell time of 10 ms for ^{43}Ca, 2.5 ms for ^{55}Mn, ^{88}Sr, ^{139}La, ^{140}Ce, ^{147}Sm, ^{153}Eu, ^{157}Gd, ^{175}Lu, ^{208}Pb

and ^{232}Th, 5 ms for ^{175}Lu, and a longer dwell time of 25 ms for ^{206}Pb, ^{207}Pb, and ^{238}U. Although Cl can exhibit a strong control on apatite fission-track annealing kinetics (Green et al., 1986; Barbarand et al., 2003) and can be analysed by LA-Q-ICP-MS (Chew et al., 2014a), its elevated background and high first ionisation energy result in low signal/background ratios which makes it challenging to measure with the short dwell times employed in the LA-Q-ICP-MS grain-mapping approach. Chlorine was therefore not monitored in this study.

3.2 Data Reduction

We imported and reduced the data in Iolite v2.5 (Paton et al., 2010; 2011). Iolite synchronises the ICP-MS data files and laser log files to define individual standard and unknown analyses (termed "integrations" within Iolite). When defining the integrations in Iolite, the first and last 2 s of the primary reference materials NIST 612 and Madagascar apatite signals were systematically cropped, while 1 s was cropped of McClure Mountain apatite signal due to its small grains. The "Dur_zeta" and the unknown apatite signals were not cropped during that step; their entire signal was used to produce map with Monocle (see the Extracting data with Monocle section 3.3), as a polygon selecting the counted area is subsequently drawn inside the image so no cropping of signals is necessary. All integrations of the primary reference materials were further manually adjusted if needed before applying the data reduction schemes. The baseline integration (background signal) was defined using the latter portion of the 10 s washout intervals; a smooth spline line was subsequently fitted to these baseline data which were then subtracted from the standard and unknown signals.

Fission-track data (i.e. U/Ca ratios) were reduced using a "Trace_Elements_FTD" data reduction scheme (DRS) and employing semi-quantitative standardisation following Chew and Donelick (2012) and Cogné et al. (2020). NIST 612 SRM silicate glass was used as the primary LA-ICP-MS reference material and previously counted Durango apatite (the "Dur_zeta" mount) as the zeta reference material (see supplementary data table SD1). Uranium concentrations were subsequently normalized relative to ^{43}Ca to correct for variations in ablation yield. We reduced the trace and rare-earth element data using the Iolite "Trace_Elements" DRS with NIST 612 as the primary reference material and with ^{43}Ca as an internal elemental standard (the "Dur_zeta" grains are used as the quality control material for these data, see supplementary data table SD2).

U-Pb data were reduced using the “VisualAge_UcomPbine” DRS (Chew et al., 2014b), which is a modified version of the “Vizual Age” DRS of Petrus and Kamber (2012) that can correct for the presence of Pb_c in the primary standard. Here, the DRS was run with a ^{207}Pb-based correction applied to the primary standard and with a linear downhole fractionation correction of zero slope which is appropriate for a shallow rastering approach as time-resolved U/Pb fractionation is absent in line scans (Košler and Sylvester, 2003). Madagascar apatite (U-Pb dated at 473.5 ± 0.7 Ma; Cochrane et al., 2014) was used as the primary matrix-matched standard for reducing the apatite U-Pb data. The quality control materials are Durango apatite and McClure Mountain apatite (523.51 ± 1.47 Ma $^{207}Pb/^{235}U$ ID TIMS age; Schoene and Bowring, 2006). The secondary U-Pb reference material data are reported in the U-Pb supplementary data table SD3.

3.3 Extracting data with Monocle

Iolite generates X-Y maps by converting each time-resolved data point of a channel computed by a DRS (e.g., $^{238}U/^{43}Ca$) into a pixel using Igor Pro’s “Gizmo” Open GL visualisation tool (Paton et al., 2011; Fig. 2). In this study, as all maps were acquired by horizontal rasters with a 18 µm laser beam, the pixels are 18 µm high with a 3.5 µm width, which corresponds to the ICP-MS total sweep time (140.5 ms) times the laser scan speed (25 $µm.s^{-1}$, Table 1). The recently developed Iolite add-on Monocle (Petrus et al., 2017) facilitates display and interrogation of Iolite maps using a flexible “data-extractor” tool. In this study we extracted data from a user-defined polygon, which closely mimics the area counted for fission-tracks. To match the polygon with the counted area, the polygon is defined using the $^{238}U/^{43}Ca$ map and aligned with the picture of the counted grain (Fig. 2a). The $^{238}U/^{43}Ca$ map also allows for identification of any zircon inclusions (which would yield high U but no Ca) which are then excluded from the polygon.

While Monocle displays one channel (an elemental abundance or an isotopic ratio) on a map at a time, the “data-extractor” tool retrieves average values for all pixels within the user-defined area for the full suite of channels computed by each different DRS. The Monocle plug-in automatically compiles all extracted average values in an exportable table with their associated internal standard errors.

3.4. Age calculation

3.4.1 Apatite fission-track ages

Apatite FT age calculation is performed offline using the information from the Monocle and TrackWorks exported datafiles and employs the Windows Excel spreadsheet provided by Cogné et al. (2020). We refer the reader to the study of Cogné et al. (2020) for further details about the zeta-based calibration and AFT age calculation. In this study, the zeta-factor was obtained using 70 Durango apatite shards analysed during a “primary zeta” session and is 0.70 ± 0.03 (zeta-factor of C.A.).

During each of the seven grain-mapping analytical sessions undertaken in this study, a pool of 15 of those 70 Durango apatite shards were revisited and analysed. Their respective mean $^{238}U/^{43}Ca$ values extracted with Monocle, and the N_s and counted-area values exported from TrackWorks, are imported into the Cogné et al. (2020) spreadsheet. This spreadsheet calculates (i) a session-specific fractionation factor (R_i ratio) which accounts for systematic variations in the $^{238}U/^{43}Ca$ values of Durango apatite shards between the “primary zeta” session and the analytical sessions where FT unknowns are measured and which is related to variations in the ICP-MS tuning conditions, (ii) single and pooled AFT ages of the shards and (iii) single and pooled AFT ages of the unknowns (see supplementary data table SD1). As the mapping approach employs a shallow ablation down to c. 3 µm, the $^{238}U/^{43}Ca$ ratio is not depth-weighted, which is the only modification in this study made to the approach of Cogné et al. (2020).

We used IsoplotR (Vermeesch, 2008) to display all the single-apatite FT ages of each sample on radial plots (Fig. 3, left panels). The central AFT age of each sample is calculated by IsoplotR and is reported in Figure 3 and Table 2; the pooled AFT age is reported when sample passes the χ^2 test ($P(\chi^2) > 0.05$), which suggests one main age population (e.g., Galbraith 1990; Vermeesch, 2017). The uncertainties are given at the 2σ level.

3.4.2 Apatite U-Pb ages

U-Pb data extracted with Monocle are imported into the Isoplot 4.15 add-in for Excel (Ludwig, 2012) to propagate uncertainties (following Horstwood et al., 2016 and Drost et al., 2018) and carry out age calculations and plotting. The $^{207}Pb/^{206}Pb$ *vs* $^{238}U/^{206}Pb$ data are plotted on a Tera-Wasserburg

Concordia plot through which a linear regression is fitted to obtain a lower intercept $^{238}U/^{206}Pb$ age. The upper intercept is anchored either with a known initial $^{207}Pb/^{206}Pb$ as for the Fish Canyon Tuff apatite ($^{207}Pb/^{206}Pb$: 0.8444 ± 0.0006; Hemming and Rasbury, 2000), or with a $^{207}Pb/^{206}Pb$ initial value derived from the Stacey and Kramers (1975) terrestrial Pb evolution model, as for Durango apatite ($^{207}Pb/^{206}Pb$: 0.84 ± 0.01). Anchoring Tera-Wasserburg regressions using the Stacey and Kramers (1975) terrestrial Pb evolution model may not always be appropriate in Cenozoic samples as the amount of radiogenic Pb in-growth in such young samples is typically not significant and the regression will likely be heavily dependent on the choice of the initial $^{207}Pb/^{206}Pb$ ratio. We therefore calculated the lower intercept U-Pb ages of the unknowns with an unanchored Model 1 fit to the array. Lower intercept dates are reported with a 95% confidence level (see Table 3 which also includes information on the uncertainty propagation).

4. Results

4.1 Apatite fission-track ages

Except for the Durango, Fish Canyon Tuff and RC2168 apatites, most of the bedrock apatite samples analysed in this study have low fission-track densities (< 1.10^5 tracks.cm^{-2}; Table 2). Detecting U zonation in these apatites was thus impossible when inspecting their spontaneous fission-track distributions. In sample RM13 from Paros in particular, the grain-mapping method reveals complex U/Ca zonation (and thus U zonation as Ca is assumed stoichiometric) undetected under the microscope, which shows that the FT grain-mapping protocol employed in this study closely emulates the role of the muscovite detector employed in the EDM approach (Fig. 2b).

All apatite samples yield similar pooled and central FT ages at the 2σ level. Five samples pass the $P(\chi^2)$ test, while four do not, independent of the nature of their protolith (Table 2). When compared to their literature constraints, all AFT ages obtained from the grain mapping approach are indistinguishable from their adopted AFT ages within 2σ uncertainties; the Durango and Fish Canyon Tuff apatite samples yield pooled FT ages of 29.1 ± 1.6 Ma and 26.6 ± 2.0 Ma, respectively (Fig. 3a, b, left panels). The sole exception arises for samples him610/205 and him622/244, for which an age discrepancy occurs between the central AFT ages obtained in this study (1.04 ± 0.05 Ma and 0.8 ± 0.3 Ma, respectively) and those published in Treloar et al (2000; 1.7 ± 0.2 Ma and 0.03 ± 0.04 Ma, respectively; Table 2). No AFT age was reported for the RM13 sample, but the central AFT age obtained in this study (9.9 ± 0.6 Ma; n=78) agrees with central AFT_{EDM} ages from Paros that range between 12.5 ± 2.8 and 10.5 ± 2.0 Ma (Brichau et al., 2006). Finally, the central and pooled AFT ages obtained from sample RC2168 (312 ± 23 and 306 ± 17, respectively) are in very good agreement with those (316 ± 38 and 309 ± 26; respectively) obtained by Döpke (2017; Table 2) with the spot ablation approach. Sample RC2168, unlike the samples which yield very young AFT ages, better illustrates the precision of our mapping approach.

4.2 Apatite U-Pb ages

All U-Pb ages are presented in Table 3; the first age-associated uncertainty corresponds to the session-wide estimate (quadratic addition of internal uncertainties and overdispersion of NIST612 data), while the second uncertainty is the overall propagated systematic uncertainty including the uncertainty on the Madagascar apatite reference age, the ^{238}U decay constant uncertainty and a 7% uncertainty derived from the U-Pb results of the “Dur_zeta” shards analysed in all seven sessions. For Durango, Fish Canyon Tuff, RM13 and RC2168 apatite samples with known U-Pb ages, the data extracted from Monocle yield lower intercept $^{238}U/^{206}Pb$ ages of 29.2 ± 1.7 / 2.7 Ma (MSWD= 2.1), 30.9 ± 2.7 / 3.5 Ma (MSWD= 2.0), 10.9 ± 2.0 / 2.1 Ma (MSWD= 1.4), and 495 ± 16 / 37 Ma (MSWD= 1.8), respectively (Fig. 3a, b, i, middle panels), which are in good agreement with their literature constraints (Table 3).

The U-Pb age of sample hb3197 is hampered by low $^{238}U/^{206}Pb$ ratios with limited spread, and thus yields an uncertainty >100 % (95% confidence, 9 ± 13 / 13 Ma, MSWD= 3.1; Table 3). The U-Pb age of sample hb4396 (1795 ± 42 / 117 Ma; MSWD= 11) corresponds to the age of the Wangtu Gneiss Complex (Chambers et al., 2008; Kohn et al., 2010) implying that regional Miocene metamorphism of the Lesser Himalayan Crystalline Sequence did not reset the Paleoproterozoic U-Pb age of the hb4396 apatite. We note that for the hb4396 sample the MSWD is high, thus highlighting age dispersion.

The lower intercept $^{238}U/^{206}Pb$ ages of apatite samples him610/205, him618/230 and him622/244 are 21.6 ± 4.2 / 4.5 Ma (MSWD= 15), 3.4 ± 8.0 / 8.0 Ma (MSWD= 4.8) and 6.7 ± 4.6 / 4.6 Ma (MSWD= 3.8), respectively (Fig.3f, g, h, middle panels). The U-Pb age of him610/205 apatites is coherent with the 27 ± 1 Ma hornblende Ar/Ar age obtained on that sample by Treloar et al. (2000). The 95% confidence level uncertainties associated with sample him618/230 and him622/244 are large (>100% and 69%, respectively) due to the limited spread in $^{238}U/^{206}Pb$ ratios leading to poor U-Pb age precision, although they are coherent with the late Miocene Ar-Ar cooling ages reported in the Nanga Parbat massif in Zeitler et al. (2001, see Section 2.1). The him-apatite samples also display large MSWDs.

4.3 Trace and rare-earth element contents

Trace and rare-earth element data from Monocle were normalised against chondrite values from McDonough and Sun (1995) and plotted in multi-element spectra diagrams (Fig. 3, right panels). The 26 spectra obtained from Durango apatite show no dispersion and are in excellent agreement with the solution ICP-MS values of Chew et al. (2016) from the same crushed Durango crystal aliquots (Fig. 3a, right panel). The 29 spectra obtained on the Fish Canyon Tuff apatite have limited dispersion and the chondrite-normalised La, Ce, Sm, Eu, Gd and Lu values agree with that obtained by LA-ICP-MS analysis by Pang et al. (2017; Fig. 3b, right panel). The 78 spectra obtained from RM13 Paros apatite agree with the mean spectrum obtained by Henrichs et al. (2018; Fig. 3c, right panel), and we obtain the same range of chondrite-normalised Th and U values with those reported in that study (Table 4). These results show that the grain-mapping approach achieves accurate and precise measurement of trace and rare earth elements.

We note that several of the hb- and him-apatite samples have scattered trace element spectra implying different grain populations (Fig. 3d to h, right panel), although there are no trace element spectra for these samples in the literature to compare our results with. Nonetheless, we explore the trace element chemistry of these samples to extract host rock-type information (e.g. igneous *vs* metamorphic apatite, which can aid U-Pb data interpretation) using the apatite trace element database compiled from a suite of distinct bedrock lithologies by O'Sullivan et al. (2020). A subset of this database is investigated using principal component analysis (PCA) with the following input variables: Sr, La, Sm, Lu and Eu/Eu* ($Eu/Eu^* = Eu_N/(Sm_N{*}Gd_N)^{0.5}$; where N = chondrite-normalised). The PCA plot (Fig. 4) shows that most of the hb- and him-samples (except hb4396) plot in the high-grade metamorphic and S-type granite fields, with samples hb3197 and him622/244 trending towards the low-grade metamorphic field. Sample hb4396 plots in the igneous apatite (I-type and mafic igneous) category along with sample RC2168 (Fig. 4).

5. Discussion

5.1 Apatite fission-track data

The AFT ages obtained with the LA-Q-ICP-MS mapping technique reproduce well with the literature constraints within 2σ uncertainty. The AFT pooled age precision is ≤7.5 % for the Durango, Fish Canyon Tuff, RM13 Paros and RC2168 samples, and range from 9 to 50% for the youngest (<2 Ma) samples (Table 2).

Samples him610/205 and him622/244 are two samples with an AFT age discrepancy between the central ages obtained and their published age constraints (Table 2). Here we tested whether it is possible to reproduce the EDM central ages of him610/205 and him622/244 samples within 2σ uncertainty using twenty grains (i.e., the number of grains counted in Treloar et al., 2000). We produced an in-house R-script which picks a set of 20 grains at random from our dataset and calculates a central age for this grain subset using IsoplotR. This R-script runs for 1000 iterations and then calculates the percentage of runs whose central ages overlap within 2σ uncertainty with the published age constraints for samples him610/205 and him622/244 listed in Table 2. Using this R-script, 0.1 and 4.3 % of runs overlap within 2σ age uncertainty for him610/205 and him622/244, respectively. The small number of runs that overlap within 2σ age uncertainty suggest that the discrepancy is not due to the number of grains counted and analysed in this study. The reason for this discrepancy is uncertain.

Sample him622/244 has an age dispersion of 123% due to five distinctly old single-grain FT ages (grains coloured in blue on Fig.3h; supplementary data SD1), while the other samples have age dispersion <31%; Fig.3a-g,i, left panels). According to their respective transmitted light picture, U/Ca and Ce/Ca trace element maps, these five old grains do not have inclusions. Interestingly, these five grains have the lowest chondrite-normalised trace element values (including U) and are those with the lowest $^{238}U/^{206}Pb$ ratios (Fig. 3h, middle panel). These observations imply that these five grains with low U and REE were more resistant to fission-track annealing. Although this is based only on few grains in one sample, a relationship between low U and old single-grain FT ages was also made by Glorie et al. (2017). LA-Q-ICP-MS therefore has great potential in determining the key trace elements for further investigations of FT retentivity.

5.2 Apatite U-Pb and trace element data

The U-Pb dates obtained with the grain-mapping approach on the Durango, Fish Canyon Tuff reference apatites, and sample RC2168 reproduce within 95% confidence uncertainty with their accepted U-Pb ages from LA-Q-ICP-MS spot analyses (with “session-wide” uncertainties < 10 %; Table 3). Therefore, for igneous apatites the accuracy and precision of U-Pb data is not compromised even when mapping with an 18 μm spot size. The Paros (sample RM13) and Himalayan (hb- and him- samples suite) apatites yield greater uncertainties at the 95% confidence level (all >10 % except hb4396; Table 3). These samples are relatively young metamorphic apatites (Fig. 4) characterised by low $^{238}U/^{206}Pb$ ratios (high Pb_c to radiogenic Pb ratios) with a limited spread on Tera-Wasserburg concordia (Fig. 3), which results in poorer precision on the resultant U-Pb age (Henrichs et al., 2018).

Most of the Himalayan apatite sample U-Pb ages are dispersed with large MSWDs (Fig. 3), which based on their scattered trace element spectra could be related to distinct grain populations (e.g. neocrystalline metamorphic apatite and relict higher-grade or magmatic porphyroclasts). Isolating apatite grain populations based on trace-element composition can reduce the U-Pb data dispersion within a sample (Henrichs et al., 2018). This was not undertaken as it was not the primary goal of this study; only one grain (#31, sample him610/205) was excluded from a Tera-Wasserburg concordia plot due to its highly distinctive trace element spectrum compared to other analyses (Fig. 3f).

5.3 Advantages and limitations

The elemental mapping method presented herein provides a new approach for laboratories undertaking AFT dating by LA-Q-ICP-MS to deal with low fission-track density apatite grains, while maintaining good age precision. As a result, the entire spectrum of low through to high spontaneous fission-track density grains encountered in natural apatite samples can now be analysed by the same LA-ICP-MS instrument without resorting to the EDM with its associated time-consuming irradiation step. Additionally, our approach not only yields accurate and precise AFT dates of low fission-track density apatite grains, but also facilitates simultaneous and accurate U-Pb dating and trace element determinations on the same samples (Fig. 3). While the elemental mapping approach is admittedly slower than single spot ablations, it is still faster than the EDM as it removes the need for sample irradiation and cooling, mica etching and induced fission-track counting on the mica and dosimeter glasses. Compared to spot ablations, as the whole grain is used to count spontaneous fission-tracks and extract ICPMS data, the siting of the counting area is no longer an issue.

5.4 Recommendations for future work

Below we list a series of recommendations for apatite LA-ICP-MS fission-track mapping studies.

1. Rectangular ablation areas (with edges aligned “N-S” and “E-W”) are the simplest to define in most laser ablation software packages, and greatly simplify subsequent data reduction. Apatite grains should therefore be mounted parallel to each other on the grain mounts and their c-axes aligned “N-S” or “E-W” within the sample holder, as this minimizes the amount of epoxy analysed within the rectangular area of ablation.
2. Orientating the line scans parallel to the grain c-axis results in longer rasters and thus best resolves the spatial elemental distribution. Orientating the line scans perpendicular to the c-axis would result in more line scans, which increases the analysis duration as each line scan is followed by a fixed washout interval.
3. Improving the washout in the laser ablation cell (e.g. by using an aerosol rapid introduction system such as in this study) shortens the analysis duration. This is because faster laser stage translation is possible as smearing is reduced, while the washout interval after every line scan can be shortened. If a low dispersion (i.e. fast washout) cell, as employed in this study, is not available then either the scan speed can be reduced, or the aerosol transfer tubing shortened to reduce signal smearing.
4. Our AFT LA-ICP-MS mapping approach is tailored for samples with low spontaneous fission-track densities. For such samples, we advocate, similar to McDannell et al. (2019), analysing significantly more than twenty grains (e.g. n ≥40) per sample to improve age accuracy and precision.

5. In this study, mean values (e.g. U/Ca and U/Pb ratios and other trace elements) were obtained over the entire grain surface. While we did not isolate and pool pixels from the grain maps, it is possible to isolate homogeneous chemical domains on age maps using Monocle (Petrus et al., 2017; Drost el al., 2018) to link apatite U-Pb dates with texturally controlled petrographic elemental information.

6. Conclusions

This work presents an LA-Q-ICP-MS analytical protocol to produce micron-scale elemental ratio maps for fission-track dating of apatite. The protocol is specifically designed for samples with low fission-track density (≤ $1x10^5$ tracks.cm^{-2}), which can be problematic for LA-Q-ICP-MS ablation spot analysis as potential U zoning cannot be detected. Our approach produces accurate and precise fission-track dates for Durango and Fish Canyon Tuff, a suite of previously dated samples (six igneous and metamorphic bedrock samples with young AFT ages), and an apatite sample with old AFT age with high fission-track density and known U zonation. The method yields two-dimensional U concentration distributions for the top c. 3 μm of the grain surface (which incorporates >50% of etched spontaneous fission-tracks). Although this assumption could be invalidated in the rare case of a sample with appreciable, non-systematic μm-scale U zoning with depth, the mapping method appears a reliable alternative approach to fission-track dating of apatite with low U contents and/or young fission-track ages by LA-Q-ICPMS without resorting to the time-consuming EDM. Additionally, the method produces U-Pb dates and trace element abundances (Mn, Sr, La, Ce, Sm, Eu, Gd, Lu), which for all samples reproduce with literature constraints (when available) within 95% confidence level.

Finally, the high-resolution imaging protocol integrated with Monocle offers the possibility to isolate pixels of homogeneous chemical domains over large crystals (e.g., Drost et al., 2018). This approach has already been applied to metamorphic apatite petrogenesis study (Henrichs et al., 2019), and has further potential for bioapatite (e.g., bones and teeth) chemical mapping, where it would be particularly suited to identifying and isolating zones affected by diagenesis to improve U-series dating of fossil bioapatite materials.

Acknowledgements

C.A. thanks Isadora Henrichs and Andy Carter for sharing the Paros and western Himalayan apatite separates respectively, Chris Mark for helpful discussion on apatite U-Pb dating, and Leona O'Connor for the white light interferometer analyses. The authors thank Stijn Glorie and Murat Tamer for their detailed reviews of this manuscript, Balz Kamber for his editorial handling, Nathan Cogné for his comments on an early draft and Foteini Drakou for her assistance with the LA-ICP-MS mapping of sample RC2168. This research is supported by a research grant from Science Foundation Ireland under Grant Number 13/RC/2092, which is co-funded under the European Regional Development Fund and by PIPCO RSG and its member companies.

References

Barbarand, J., Carter, A., Wood, I., Hurford, T., 2003. Compositional and structural control of fission-track annealing in apatite. Chemical Geology, v. 198, pp. 107-137. doi :10.1016/S0009-2541(02)00424-2

Belousova, E.A., Griffin, W.L., O'Reilly, S.Y., Fisher, N.I., 2002a. Apatite as an indicator mineral for mineral exploration: Trace-element compositions and their relationship to host rock type. Journal of Geochemical Exploration, v. 76, pp. 45–69. https://doi.org/10.1016/S0375-6742(02)00204-2.

Brichau, S., Ring, U., Ketcham, R.A., Carter, A., Stockli, D., Brunel, M., 2006. Constraining the long-term evolution of the slip rate for a major extensional fault system in the central Aegean, Greece, using thermochronology. Earth and Planetary Science Letters, v. 241, pp. 293-306. doi :10.1016/j.epsl.2005.09.065

Caddick, M.J., Bickle, M.J., Harris, N.B.W., Holland, T.J.B., Horstwood, M.S.A., Parrish, R.R., Ahmad, T., 2007. Burial and exhumation history of a Lesser Himalayan schist: recording the formation of an inverted metamorphic sequence in NW India. Earth and Planetary Science Letters, v. 264, pp. 375-390. doi :10.1016/j.epsl.2007.09.011

Chambers, J.A., Argles, T.W., Horstwood, M.S.A., Harris, N.B.W., Parrish, R.R., Ahmad, T., 2008. Tectonic implications of Palaeoproterozoic anatexis and Late Miocene metamorphism in the

Lesser Himalayan Sequence, Sutlej Valley, NW India. Journal of the Geological Society, London, v. 165, pp. 725-737.

Chew, D., Donelick, R.A., 2012. Combined apatite fission track and U-Pb dating by LA-ICP-MS and its application in apatite provenance analysis. Mineralogical Association of Canada Short Course 42, pp. 219-247.

Chew, D.M., Donelick, R.A., Donelick, M.B., Kamber, B.S., Stock, M., 2014a. Apatite chlorine concentration measurements by LA-ICP-MS. Geostandards and Geoanalytical Research, v. 38, pp. 23-35. doi:10.1111/j.1751-908X.2013.00246.x.

Chew, D.M., Petrus, J.A., Kamber, B.S., 2014b. U–Pb LA–ICPMS dating using accessory mineral standards with variable common Pb. Chemical Geology, v. 363, pp. 185–199. doi:10.1016/j.chemgeo.2013.11.006.

Chew D.M., Babechuk, M.G., Cogné, N., Mark, C., O'Sullivan, G., Henrichs, I.A., Doepke, D., McKenna, C., 2016. (LA, Q)-ICPMS trace-element analyses of Durango and McClure Mountain apatite and implications for making natural LA-ICPMS mineral standards. Chemical Geology, v. 435, pp. 35–48. doi: 10.1016/j.chemgeo.2016.03.028

Chew D.M., Drost, K., Petrus, J., 2019. Ultrafast, > 50 Hz LA-ICP-MS spot analysis applied to U-Pb dating of zircon and other U-bearing minerals. Geostandards and Geoanalytical Research, v. 43, pp. 39-60. doi: 10.1111/ggr.12257

Cochrane, R., Spikings, R.A., Chew, D., Wotzlaw, J.F., Chiaradia, M., Tyrrell, S., Schaltegger, U., van der Lelij, R., 2014. High temperature (>350 C) thermochronology and mechanisms of Pb loss in apatite. Geochimica et Cosmochimica Acta, v. 127, pp. 39-56. https://doi.org/10.1016/j.gca.2013.11.028

Cogné, N., Chew, D.M., Donelick, R.A., Ansberque, C., 2020. LA-ICP-MS apatite fission track dating: A practical zeta-based approach. Chemical Geology, v. 531. doi:10.1016/j.chemgeo.2019.119302

Dill, H.G., 1994. Can REE patterns and U-Th variations be used as a tool to determine the origin of apatite in clastic rocks. Sedimentary Geology, v. 92, pp. 175–196. https://doi.org/10.1016/0037-0738(94)90105-8.

Donelick, R.A., Ketcham, R.A., Carlson, W.D., 1999. Variability of apatite fission-track annealing kinetics: II. Crystallographic orientation effects. American Mineralogist, v.84(9), pp.1224-1234. https://doi.org/10.2138/am-1999-0902

Donelick R.A., O'Sullivan, P., Ketcham, R.A., 2005. Apatite fission-track analysis. Reviews in Mineralogy and Geochemistry, v. 58, pp. 49-94.

Döpke, D., 2017. Modelling the thermal history of onshore Ireland, Britain and its offshore basins using low-temperature thermochronology. PhD Thesis, Trinity College Dublin.

Drost, K., Chew, D.M., Petrus, J.A., Scholze, F., Woodhead, J.D., Schneider, J.W., Harper, D.A., 2018. An image mapping approach to U-Pb LA-ICP-MS carbonate dating and applications to direct dating of carbonate sedimentation. Geochemistry, Geophysics, Geosystems, 19. https://doi.org/10.1029/2018GC007850

Galbraith, R.F., 1990. The radial plot: graphical assessment of spread in ages. Nuclear Tracks Radiation Measurement, v. 17, pp. 207-214.

Gallagher, K., Brown, R., Johnson, C., 1998. Fission track analysis and its applications to geological problems. Annual Review of Earth and Planetary Sciences, v. 26. https://doi.org/10.1146/annurev.earth.26.1.519

Glorie, S., Alexandrov, I., Nixon, A., Jepson, G., Gillespie, J., Jahn, B-M., 2017. Thermal and exhumation history of Sakhalin Island (Russia) constrained by apatite U-Pb and fission-track thermochronology. Journal of Asian Earth Sciences, v. 143, pp. 326-342. https://doi.org/10.1016/j.jseaes.2017.05.011

Green, P., 1986. On the thermo-tectonic evolution of Northern England: evidence from fission-track analysis. Geological Magazine, v.123(5), pp. 493-506. https://doi.org/10.1017/S0016756800035081

Hasebe, N., Barbarand, J., Jarvis, K., Carter, A., Hurford, A.J., 2004. Apatite fission-track chronometry using laser ablation ICP-MS. Chemical Geology, v. 207, pp. 135-145. https://doi.org/10.1016/j.chemgeo.2004.01.007

Hasebe, N., Tamura, A., Arai, S., 2013. Zeta equivalent fission-track dating using LA-ICP-MS and examples with simultaneous U-Pb dating. Island Arc, v. 22(3), pp. 280-291. https://doi.org/10.1111/iar.12040

Hemming, S.R. and Rasbury, E.T., 2000. Pb isotope measurements of sanidine monitor standards: implications for provenance analysis and tephrochronology. Chemical Geology, v. 163(3-4), pp. 331-337. https://doi.org/10.1016/S0009-2541(99)00174-6

Henrichs, I.A., O'Sullivan, G.J., Chew, D.M., Mark, C., Babechuk, M.G., McKenna, C., Emo R., 2018. The trace element and U-Pb systematics of metamorphic apatite. Chemical Geology, v.483, pp. 218-238. https://doi.org/10.1016/j.chemgeo.2017.12.031

Henrichs, I.A., Chew, D.M., O'Sullivan, G.J., Mark, C., McKenna, C., Guyett, P., 2019. Trace element (Mn-Sr-Y-Th-REE) and U-Pb isotope systematics of metapelitic apatite during progressive greenshist- to amphibolite-facies barrovian metamorphism. Geochemistry, Geophysics, Geosystems, v. 20(8), pp. 4103-4129. https://doi.org/10.1029/2019GC008359

Horstwood, M.S.A., Kosler, J., Gehrels, G., Jackson, S.E., McLean, N., Paton, C., Pearson, N.J., Sircombe, K., Sylvester, P., Vermeesch, P., Bowring, J.F., Condon, D.J., Schoene, B., 2016. Community-Derived standards for LA-ICP-MS U-(Th-)Pb geochronology – Uncertainty Propagation, Age Interpretation and Data Reporting. Geostandards and Geoanalytical Research, v. 40 (3), pp. 311-332. doi: 10.1111/j.1751-908X.2016.00379.x

Hurford, A.J., and Green, P., 1982. A users' guide to fission track dating calibration. Earth and Planetary Science Letters, v. 59, pp. 343-354. https://doi.org/10.1016/0012-821X(82)90136-4

Kohn, M.J., Paul, S.K., Corrie, S.L., 2010. The lower Lesser Himalayan sequence: A Paleoproterozoic arc on the northern margin of the Indian plate. GSA Bulletin, v. 122(3-4), pp. 323-335. https://doi.org/10.1130/B26587.1

Košler, J. and Sylvester, P.J., 2003. Present trends and the future of zircon in geochronology: Laser ablation ICPMS. Reviews in Mineralogy and Geochemistry, v. 53(1), pp. 243-275. https://doi.org/10.2113/0530243

Ludwig, K.R., 2012. User's manual for isoplot 3.75. Berkley Geochronology Center Special Plublication, v. 5, pp. 75.

Malusà, M.G., Fitzgerald, P.G., 2019. Fission-track thermochronology and its application to geology. Springer, Cham. https://doi.org/10.1007/978-3-319-89421-8

McDannell, K.T., Issler, D.R., O'Sullivan, P.B., 2019. Radiation-enhanced fission-track annealing revisited and consequences for apatite thermochronometry. Geochimica et Cosmochimica Acta, v. 252, pp. 213-239. https://doi.org/10.1016/j.gca.2019.03.006

McDonough, W.F., and Sun, S-s., 1995. The composition of the Earth. Chemical Geology, v. 120, pp. 223-253. https://doi.org/10.1016/0009-2541(94)00140-4

McDowell, F.W., McIntosh, W.C., Farley, K.A., 2005. A precise 40Ar–39Ar reference age for the Durango apatite (U–Th)/He and fission-track dating standard. Chemical Geology, v.214(3-4), pp. 249-263. https://doi.org/10.1016/j.chemgeo.2004.10.002

Müller, W., Shelley, M., Miller, P., Broude, S., 2008. Initial performance metrics of a new custom-designed ArF excimer LA-ICPMS system coupled to a two-volume laser ablation cell. Journal of Analytical Atomic Spectrometry, v. 24, pp. 209-214. https://doi.org/10.1039/B805995K

O'Sullivan, G.O., Chew, D., Kenny, G., Henrichs, I., Mulligan, D., 2020. The trace element composition of apatite and its application to detrital provenance studies. Earth-Science Reviews, v. 201. https://doi.org/10.1016/j.earscirev.2019.103044

Pang, J., Zheng, D., Ma, Y., Wang, Y., Wu, Y., Wan, J., Yu, J., Li, Y., Wang, Y., 2017. Combined apatite fission-track dating, chlorine and REE content analysis by LA-ICPMS. Science Bulletin, v. 32(22), pp. 1497-1500. https://doi.org/10.1016/j.scib.2017.10.009

Paton, C., Woodhead, J.D., Hellstrom, J.C., Hergt, J.M., Greig, A., Maas, R., 2010. Improved laser ablation U-Pb zircon geochronology through robust downhole fractionation correction. Geochemistry, Geophysics, Geosystems, v. 11(3). https://doi.org/10.1029/2009GC002618

Paton, C., Hellstrom, J.C., Paul, B., Woodhead, J., Hergt, J., 2011. Iolite: Freeware for the visualisation and processing of mass spectrometric data. Journal of Analytical Atomic Spectrometry, v. 26, pp. 2508-2518. https://doi.org/10.1039/C1JA10172B

Petrus, J.A., and Kamber, B.S., 2012. VizualAge: A novel approach to laser ablation ICP-MS U-Pb geochronology data reduction. Geostandards and Geoanalytical Research, v. 36, pp. 247-270. https://doi.org/10.1111/j.1751-908X.2012.00158.x

Petrus, J.A., Chew, D.M., Leybourne, M.I., Kamber, B.S., 2017. A new approach to laser-ablation inductively coupled-plasma mass-spectrometry (LA-ICP-MS) using a flexible map interrogation tool "Monocle". Chemical Geology, v. 463, pp. 76-93. https://doi.org/10.1016/j.chemgeo.2017.04.027

Phillips, D., Matchan, E.L., Honda, M., Kuiper, K.F., 2017. Astronomical calibration of 40Ar/39Ar reference minerals using high-precision, multi-collector (ARGUSVI) mass spectrometry. Geochimica et Cosmochimica Acta, v. 196(1), pp. 351-369. http://dx.doi.org/10.1016/j.gca.2016.09.027

Schoene, B. and Bowring, S.A., 2006. U-Pb systematics of the McClure Mountain syenite: thermochronological constraints on the age of the 40Ar/39Ar standard MMhb. Contributions to Mineralogy and Petrology, v. 151. https://doi.org/10.1007/s00410-006-0077-4

Spiegel, C. Kohn B., Raza, A., Rainer, P., Gleadow, A., 2007. The effect of long-term low-temperature exposure on apatite fission-track stability: A natural annealing experiment in the deep ocean. Geochimica et Cosmochimica Acta, v. 71, pp. 4512-4537. https://doi.org/10.1016/j.gca.2007.06.060

Sha, L.-K., Chappell, B.W., 1999. Apatite chemical composition, determined by electron microprobe and laser-ablation inductively coupled plasma mass spectrometry, as a probe into granite petrogenesis. Geochimica and Cosmochimica Acta, v. 63, pp. 3861–3881. https://doi.org/10.1016/S0016-7037(99)00210-0.

Stacey, J.S., and Kramers, J.D., 1975. Approximation of terrestrial lead isotope evolution by a two-stage model. Earth and Planetary Science Letters, v. 26, pp. 207-221.

Tagami, T., and O'Sullivan, P.B., 2005. Fundamentals of fission-track thermochronology. Reviews in Mineralogy & Geochemistry, v. 58(1), pp. 19-47. https://doi.org/10.2138/rmg.2005.58.2

Tamer, M., and Ketcham, R., 2020. Is low-temperature fission-track annealing in apatite a thermally controlled process? Geochemistry, Geophysics, Geosystems, v. 21, e2019GC008877. https://doi.org/10.1029/2019GC008877

Thompson, J., Meffre, S., Maas, R., Kamenetsky, V., Kamenetsky, M., Goemann, K., Ehrig, K., Danyushevsky, L., 2016. Matrix effects in Pb/U measurements during LA-ICP-MS analysis of the mineral apatite. Journal of Analytical Atomic Spectrometry, v. 31(6). DOI: 10.1039/c6ja00048g

Treloar, P.J., Rex, D.C., Guise, P.G., Wheeler, J., Hurford, A.J., Carter, A., 2000. Geochronological constraints on the evolution of the Nanga Parbat syntaxis, Pakistan Himalaya. Geological Society of London, v. 170, pp. 137-162. doi:10.1144/GSL.SP.2000.170.01.08

Ubide, T., McKenna, C.A., Chew, D.M., Kamber, B.S., 2015. High-resolution LA-ICP-MS trace element mapping of igneous minerals: In search of magma histories. Chemical Geology, v. 409, pp. 157-168. https://doi.org/10.1016/j.chemgeo.2015.05.020

Wagner, G., and Van den Haute, P., 1992. Fission-Track Dating. Solid Earth Sciences Library, vol 6. Springer, Dordrecht. https://doi.org/10.1007/978-94-011-2478-2_7

Vannay, J.C., Grasemann, B., Rahn, M., Frank, W., Carter, A., Baudraz, V., Cosca, M., 2004. Miocene to Holocene exhumation of metamorphic crustal wedges in the NW Himalaya: Evidence for tectonic extrusion coupled to fluvial erosion. Tectonics, v. 23(1). https://doi.org/10.1029/2002TC001429

Van Malderen S.J.M., Managh, A.J., Sharp, B.L., Vanhaecke, F., 2016. Recent developments in the design of rapid response cells for laser ablation-inductively coupled plasma-mass spectrometry and their impact on bioimaging applications. Journal of Analytical Atomic Spectrometry, v. 31, pp. 423-439. doi:10.1039/C5JA00430F

Van Malderen, S.J.M., van Elteren, J.T., Šelih, V.S., Vanhaecke, F., 2018. Considerations on data acquisition in laser ablation-inductively coupled plasma-mass spectrometry with low-dispersion interfaces. Spectrochimica Acta Part B: Atomic Spectroscopy, v. 140, pp. 29-34. https://doi.org/10.1016/j.sab.2017.11.007

Vermeesch, P., 2008. IsoplotR: A free and open toolbox for geochronology. Geoscience Frontiers, v. 9, pp. 1479-1493. https://doi.org/10.1016/j.gsf.2018.04.001

Vermeesch, P., 2017. Statistics for LA-ICP-MS based fission track dating. Chemical Geology, v. 456, pp. 19-27. http://dx.doi.org/10.1016/j.chemgeo.2017.03.002

Zeitler, P.K., Chamberlain, C.P., Smith, H.A., 1993. Synchronous anatexis, metamorphism, and rapid denudation at Nanga Parbat (Pakistan Himalaya). Geology, v. 21(4), pp. 347-350. https://doi.org/10.1130/0091-7613(1993)021<0347:SAMARD>2.3.CO;2

Figures and Tables

Figure 1. a) Schematic diagram of an apatite mount illustrating the LA-Q-ICP-MS mapping process (features are not to scale). The “ablation pattern” markers serve as location reference points which can survive multiple re-polishing events which enables reuse of the Durango “zeta” mounts. They were undertaken with the following laser conditions: 2.5 $J.cm^{-2}$ fluence, 100 Hz repetition rate and 1000 shot counts. In this protocol the laser always scans from left to right and from top to bottom. b) Ablation pit depth measurements from white light interferometry, Y-axis plotted with x 6.5 vertical exaggeration. c) Example of elemental ratio ($^{238}U/^{43}Ca$) map from Monocle.

Figure 2. a) Left panel: Optical image of him610/205 grain4 with ablation lines. Middle panel: Monocle image of grain4 showing the $^{206}Pb/^{238}U$ channel (from the Visual_UcomPbine DRS). Right panel: $^{238}U/^{43}Ca$ map (from the Trace_Element_FTD DRS), which is used to define a region of interest to extract AFT, U-Pb and trace element data. b) Example of complex U/Ca zoning in grains from the RM13 Paros sample.

Figure 3. Results from the LA-Q-ICP-MS mapping. From left to right: radial plots of single-apatite FT ages (from isoplotR, Vermeesch, 2008), Tera-Wasserburg Concordia diagram (from Isoplot 4.15, Ludwig, 2012) and chondrite-normalised multi-element spectra of the analysed samples. The AFT age to be interpreted depending on $P(\chi^2)$ value is marked by a star.

Figure 4. Principal component analysis of log-normalised Sr, La, Sm, Lu ppm values and Eu/Eu* ratios of the analysed apatite samples plotted against the bedrock apatite database compiled by O’Sullivan et al. (2020). Each 95% confidence ellipse is a lithology group (the data points forming each ellipse have been removed for clarity). ALK: alkali-rich igneous rocks; HM: partial-melts/leucosomes/high-grade metamorphic rocks; IM: mafic I-type granitoids/mafic igneous rocks; LM: low- and medium-grade metamorphic rocks; UM: ultramafic rocks; S: S-type and felsic I-type granitoids.

Table 1. LA-Q-ICP-MS Operating Conditions

Laser	
Instrument	Teledyne Photon Machines Analyte Excite ArF 193nm Excimer (HelEx II Active 2-volume Cell)
Software	Chromium 2.3
Laser carrier gas	He cell: 0.25 to 0.3 L/min He cup: 0.15 to 0.1 L/min N_2: 7 to 11 mL/min
Washout and background	10 s (including 3 s laser warm up)
Energy density	2.5 J/cm^2
Spot size	18-µm circle (corresponding to the y-axis map resolution)
Rastering process	User-defined rectangle automatically populated by raster lines (without overlap).
Repetition rate	53 Hz
Scan speed	25 µm/s
Ablation pit depth	c. 3 µm
Inductively coupled plasma mass spectrometer	
Instrument	Agilent 7900 Quadrupole
Software	MassHunter 4.3
Plasma ratio frequency power	1550 W
Sample gas flow	0.60 to 0.70 L/min
Operating mode	Time-resolved analysis
Effective mass sweep time	140.5 ms
Total dwell time	112.5 ms (^{43}Ca: 10 ms; ^{55}Mn, ^{88}Sr, ^{139}La, ^{140}Ce, ^{147}Sm, ^{153}Eu, ^{157}Gd, ^{208}Pb, ^{232}Th: 2.5 ms; ^{175}Lu: 5 ms; ^{206}Pb, ^{207}Pb, ^{238}U: 25 ms) (all sessions)
Tuning conditions	ThO^+/Th^+: 0.2%; $^{44}Ca^{2+}/^{44}Ca^+$: 0.3% (on NIST 612)
Data reduction	
Primary standard	For AFT and trace element data: NIST 612 silicate glass For U-Pb data: Madagascar apatite
Quality control material	Durango apatite (see supplementary data tables)

Data Reduction Scheme	AFT data: “Trace_Elements_FTD” Trace element data: “Trace_Elements” U-Pb data: “VizualAge_UcomPbine”

Table 2. Apatite fission-track data obtained with the LA-Q-ICP-MS grain mapping approach

ADOPTED AGES			FISSION TRACK DATA								
Sample	Age ± 2σ (Ma)	Published in	n	*Ns*	Σ Area (cm^2)	ρ (tr/cm^2)	U/Ca	U (ppm)	P(χ^2)	Central age ± 2σ (Ma)	Pooled age ± 2σ (Ma)
Durango	30.6 ± 5.4	Hasebe et al., 2004*	26[#]	2958	1.2E-02	2.5E+05	5.9E-03	18	0.32	29.3 ± 1.2	29.1 ± 1.6
Fish C. Tuff	29.7 ± 3.8	Hasebe et al., 2004*	29	1088	6.5E-03	1.7E+05	4.4E-03	13	0.18	27.1 ± 1.9	26.6 ± 2.0
RM13 Paros	10.5 ± 2.0	Brichau et al., 2006+	78	1575	1.6E-02	1.0E+05	7.4E-03	22	0.00	9.9 ± 0.6	9.5 ± 0.6
HB3197 (F8)	0.7 ± 1.2	Vannay et al., 2004°	70	22	6.4E-03	3.4E+03	4.0E-03	1	0.96	2.0 ± 0.6	0.6 ± 0.3
HB4396 (F10)	1.7 ± 1.0	Vannay et al., 2004°	69	279	7.2E-03	3.9E+04	1.4E-02	44	0.23	2.2 ± 0.4	1.9 ± 0.2
HIM610/205	1.7 ± 0.2	Treloar et al., 2000°	40	639	4.4E-03	1.5E+05	1.0E-01	311	0.03	1.04 ± 0.05	1.01 ± 0.09
HIM618/230	0.4 ± 0.2	Treloar et al., 2000°	41	170	7.0E-03	2.4E+04	5.4E-02	166	0.17	0.35 ± 0.06	0.31 ± 0.05
HIM622/244	0.03 ± 0.04	Treloar et al., 2000°	70	60	1.3E-02	4.7E+03	7.0E-03	21	0.00	0.8 ± 0.3	0.5 ± 0.1
RC2168	316 ± 38	Döpke, 2017*	36	5762	2.6E-03	2.2E+06	5.3E-03	16	0.00	312 ± 23	306 ± 17

*: LA-ICP-MS spot ablation study with < 20 grains dated

+: The closest study to the RM13 Paros sample (AFT_{EDM} analysis; < 20 grains dated)

°: EDM analysis with ≤ 20 grains dated

n: number of grains analysed in this study

#: shards

Ns: sum of spontaneous fission-tracks

U (ppm): mean U content value (from internal elemental standardisation; Table 4)

P(χ^2): Probability to obtain χ^2 for ν (nb of crystals -1) degree of freedom. If P(χ^2) >0.05 then one population is present and the pooled AFT age can be used (Galbraith, 1990; Vermeesch, 2017).

Central age is calculated with isoplotR. Pooled age is calculated with the spreadsheet of Cogné et al. (2020; see Table SD1).

ζ (zeta-factor) = 0.70 ± 0.03 (CA’s zeta factor)

Table 3. Apatite U-Pb data obtained with the LA-Q-ICP-MS grain-mapping approach

ADOPTED AGES				U/Pb DATA			
Sample	Age ± 2σ (Ma)	MSWD	Published in	n	Age ± 95% conf. (Ma)*	MSWD	initial $^{207}Pb/^{206}Pb$
Durango	30.9 ± 0.8	1.0	Thompson et al., 2016⁺	26#	29.2 ± 1.7 / 2.7	2.1	0.84 ± 0.01 [1]
Fish C. Tuff	29.1 ± 0.7	1.7	Chew et al., 2014b⁺	29	30.9 ± 2.7 / 3.5	2.0	0.8444 ± 0.0006 [2]
RM13 Paros	11.5 ± 3.8°	1.9	Henrichs et al., 2018⁺	78	10.9 ± 2.0 / 2.1	1.4	0.826 ± 0.005
HB3197 (F8)	NA	NA	NA	70	9.0 ± 13 / 13	3.2	0.691 ± 0.007
HB4396 (F10)	NA	NA	NA	69	1795 ± 42 / 117	11	0.786 ± 0.081
HIM610/205	NA	NA	NA	40	21.6 ± 4.2 / 4.5	15	0.757 ± 0.071
HIM618/230	NA	NA	NA	41	3.4 ± 8.0 / 8.0	4.8	0.645 ± 0.031
HIM622/244	NA	NA	NA	70	6.7 ± 4.6 / 4.6	3.8	0.826 ± 0.009
RC2168	484 ± 21	0.8	Döpke, 2017⁺	36	495 ± 16 / 37	1.8	0.818 ± 0.053

°: U-Pb age (± 95% conf. level) calculated using a Model 1 regression from Henrich et al. (2018)'s data (see Table SD3).

⁺: LA-Q-ICP-MS spot analyses

n: number of grains analysed in this study

#: shards

*: First uncertainty: session-wide estimate (quadratic addition of internal uncertainties and overdispersion of NIST612 data). Second uncertainty: overall propagated systematic uncertainty including the uncertainty on the Madagascar apatite reference age, the ^{238}U decay constant uncertainty and a 7% uncertainty derived from the U-Pb results of the Durango zeta apatite shards analysed in all seven sessions.

MSWD: mean square of weighted deviates

[1]: anchored using Stacey and Kramers (1975) lead evolution model

[2]: anchored using Hemming and Rasbury (2000)

Table 4. Apatite trace and rare-earth element contents (in ppm) obtained with the LA-Q-ICP-MS grain-mapping approach and used in the PCA.

Sample	Th	U	La	Ce	Sr	Sm	Eu	Gd	Lu
Durango	291-491 (363)	15-23 (18)	3508-4704 (4274)	5008-6274 (5664)	491-522 (505)	187-283 (242)	17-21 (19)	164-249 (210)	6-8 (7)
Fish Canyon Tuff	25-79 (53)	7-19 (13)	1606-2755 (2160)	2876-5152 (3977)	523-612 (560)	132-257 (189)	20-37 (28)	95-187 (138)	4-8 (6)
RM13 Paros	0-17 (2)	5-81 (22)	83-300 (147)	358-1019 (578)	108-139 (114)	222-449 (291)	14-26 (18)	295-578 (371)	11-32 (17)
HB3197 (F8)	5-116 (36)	2-27 (12)	46-551 (131)	135-1632 (451)	61-76 (68)	67-739 (215)	3-16 (7)	110-1048 (367)	37-227 (120)
HB4396 (F10)	21-641 (119)	9-93 (44)	347-2382 (1284)	1058-5931 (3533)	231-459 (330)	132-601 (443)	8-44 (30)	91-405 (299)	3-12 (6)
HIM610/205	101-550 (390)	73-441 (311)	2-521 (360)	4-954 (691)	298-342 (321)	2-85 (51)	0-11 (8)	4-92 (51)	4-13 (9)
HIM618/230	2-10 (4)	126-206 (166)	106-186 (139)	474-771 (597)	106-123 (116)	227-335 (265)	6-8 (7)	253-389 (303)	15-39 (24)
HIM622/244	0-30 (2)	1-82 (21)	13-129 (32)	42-478 (117)	81-151 (102)	23-220 (65)	1-5 (3)	40-294 (106)	12-61 (31)
RC2168	9-86 (28)	4-33 (16)	875-1986 (1230)	2346-5645 (3418)	101-144 (125)	259-680 (397)	55-151 (101)	192-526 (305)	7-19 (11)

Data are given as min-max (mean). Mn concentration and quality control data are provided in Table SD2.

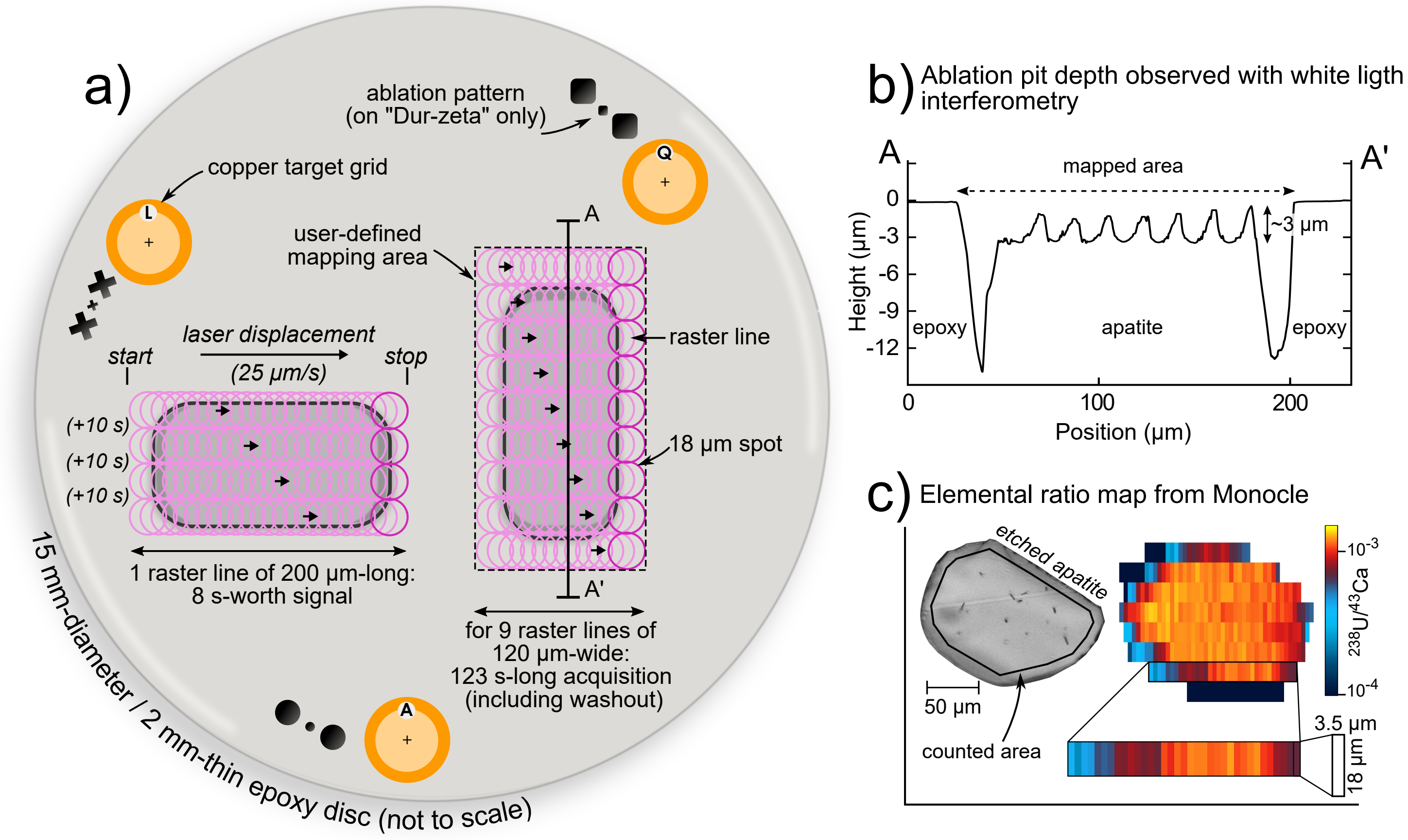

a)
ablation pattern
(on "Dur-zeta" only)
copper target grid
L
Q
A
user-defined
mapping area
A
A'
raster line
18 µm spot
laser displacement
(25 µm/s)
start
stop
(+10 s)
(+10 s)
(+10 s)
1 raster line of 200 µm-long:
8 s-worth signal
for 9 raster lines of
120 µm-wide:
123 s-long acquisition
(including washout)
15 mm-diameter / 2 mm-thin epoxy disc (not to scale)
b) Ablation pit depth observed with white ligth interferometry
A
A'
mapped area
~3 µm
epoxy
apatite
epoxy
Height (µm)
0
-3
-6
-9
-12
0
100
200
Position (µm)
c) Elemental ratio map from Monocle
etched apatite
50 µm
counted area
10^{-3}
10^{-4}
$^{238}U/^{43}Ca$
3.5 µm
18 µm

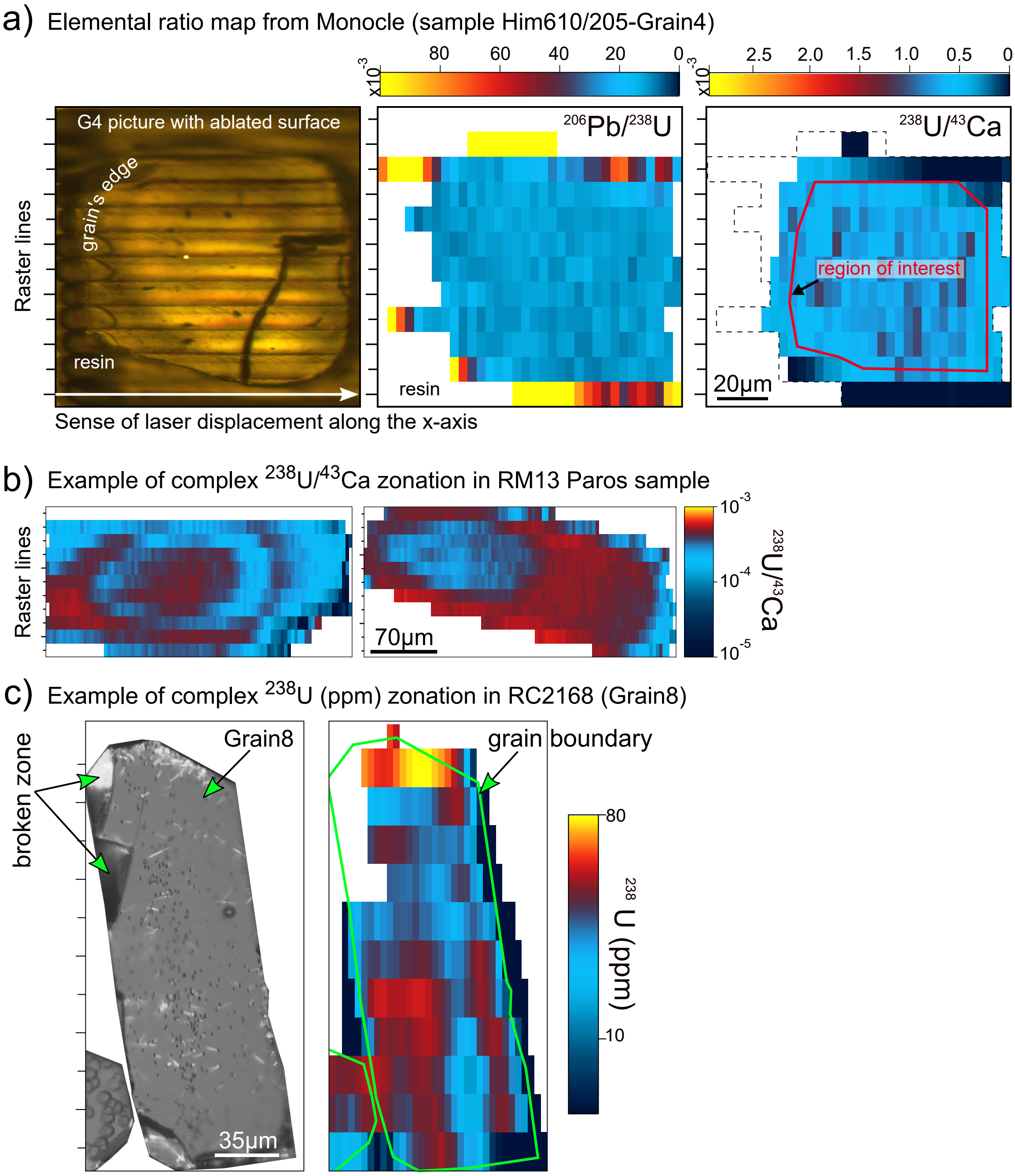

a) Elemental ratio map from Monocle (sample Him610/205-Grain4)
G4 picture with ablated surface
grain's edge
resin
Raster lines
Sense of laser displacement along the x-axis
x10-3
80 60 40 20 0
206Pb/238U
resin
x10-3
2.5 2.0 1.5 1.0 0.5 0
238U/43Ca
region of interest
20µm
b) Example of complex 238U/43Ca zonation in RM13 Paros sample
Raster lines
70µm
10-3
10-4
10-5
238U/43Ca
c) Example of complex 238U (ppm) zonation in RC2168 (Grain8)
broken zone
Grain8
35µm
grain boundary
80
10
238U (ppm)

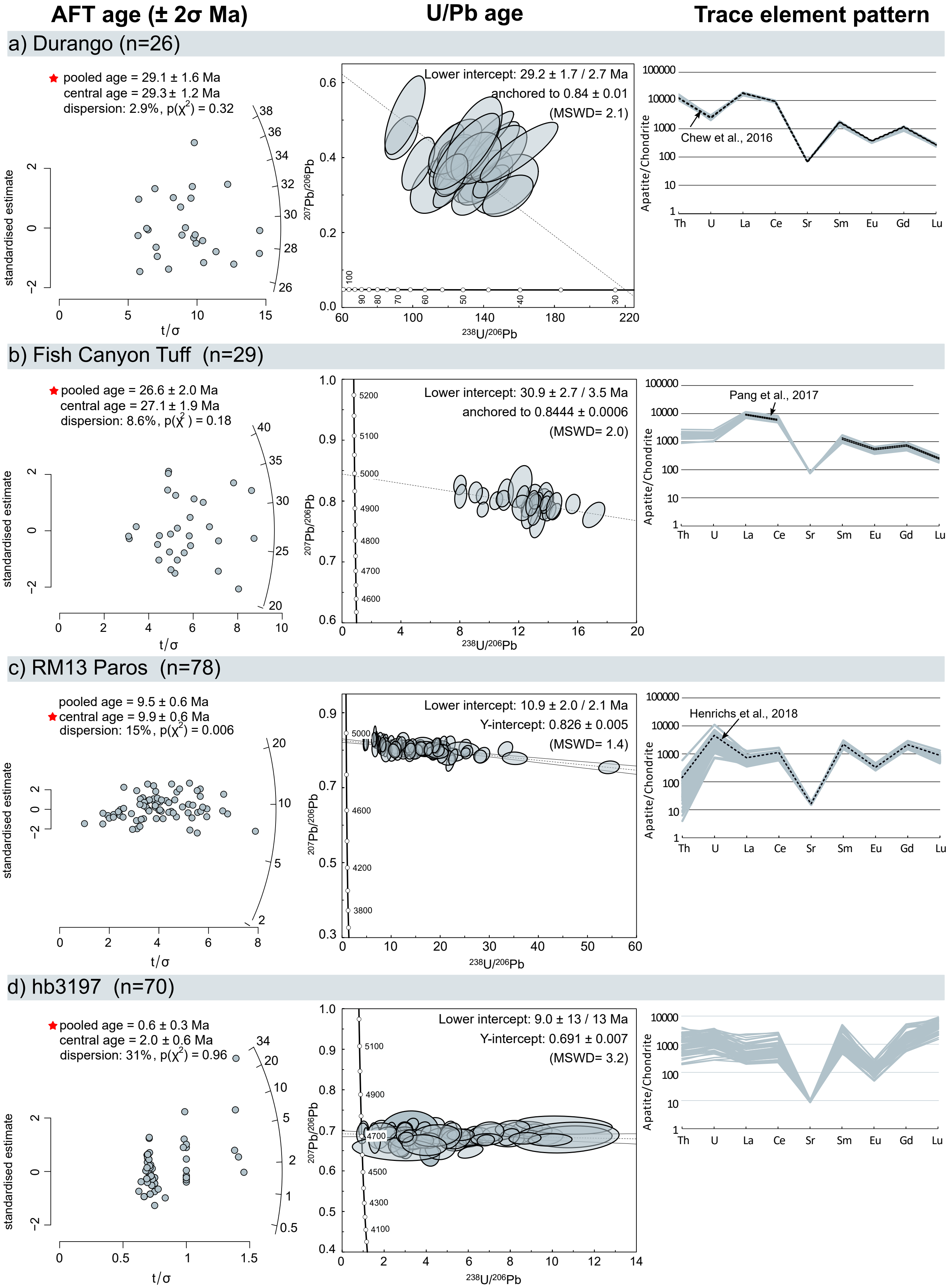
AFT age (± 2σ Ma)
U/Pb age
Trace element pattern
a) Durango (n=26)
pooled age = 29.1 ± 1.6 Ma
central age = 29.3 ± 1.2 Ma
dispersion: 2.9%, p(χ2) = 0.32
standardised estimate
t/σ
Lower intercept: 29.2 ± 1.7 / 2.7 Ma
anchored to 0.84 ± 0.01
(MSWD= 2.1)
207Pb/206Pb
238U/206Pb
Apatite/Chondrite
Chew et al., 2016
Th U La Ce Sr Sm Eu Gd Lu
b) Fish Canyon Tuff (n=29)
pooled age = 26.6 ± 2.0 Ma
central age = 27.1 ± 1.9 Ma
dispersion: 8.6%, p(χ2) = 0.18
Lower intercept: 30.9 ± 2.7 / 3.5 Ma
anchored to 0.8444 ± 0.0006
(MSWD= 2.0)
Pang et al., 2017
c) RM13 Paros (n=78)
pooled age = 9.5 ± 0.6 Ma
central age = 9.9 ± 0.6 Ma
dispersion: 15%, p(χ2) = 0.006
Lower intercept: 10.9 ± 2.0 / 2.1 Ma
Y-intercept: 0.826 ± 0.005
(MSWD= 1.4)
Henrichs et al., 2018
d) hb3197 (n=70)
pooled age = 0.6 ± 0.3 Ma
central age = 2.0 ± 0.6 Ma
dispersion: 31%, p(χ2) = 0.96
Lower intercept: 9.0 ± 13 / 13 Ma
Y-intercept: 0.691 ± 0.007
(MSWD= 3.2)

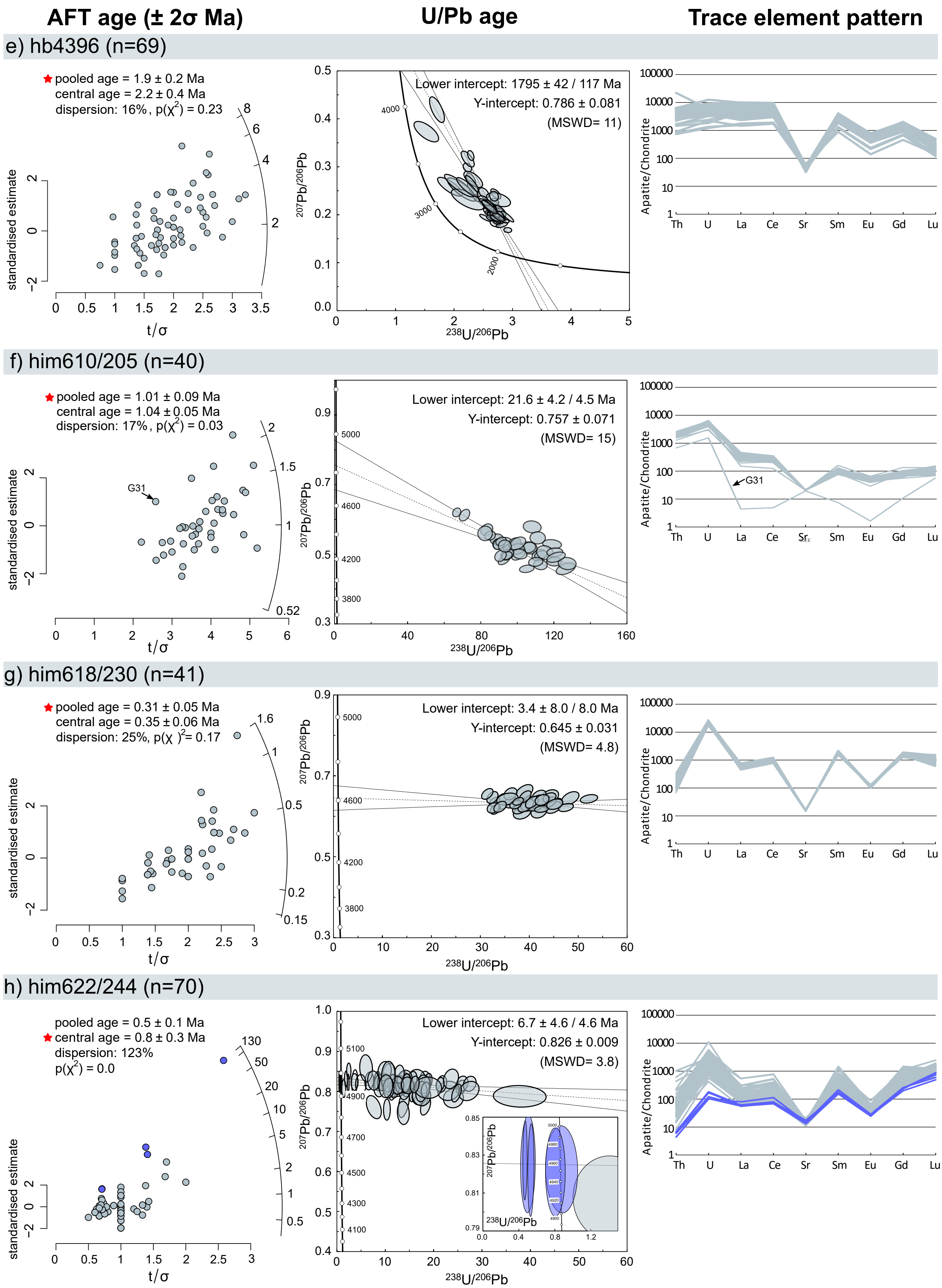

AFT age (± 2σ Ma)
U/Pb age
Trace element pattern
e) hb4396 (n=69)
pooled age = 1.9 ± 0.2 Ma
central age = 2.2 ± 0.4 Ma
dispersion: 16%, p(χ2) = 0.23
Lower intercept: 1795 ± 42 / 117 Ma
Y-intercept: 0.786 ± 0.081
(MSWD= 11)
f) him610/205 (n=40)
pooled age = 1.01 ± 0.09 Ma
central age = 1.04 ± 0.05 Ma
dispersion: 17%, p(χ2) = 0.03
G31
Lower intercept: 21.6 ± 4.2 / 4.5 Ma
Y-intercept: 0.757 ± 0.071
(MSWD= 15)
g) him618/230 (n=41)
pooled age = 0.31 ± 0.05 Ma
central age = 0.35 ± 0.06 Ma
dispersion: 25%, p(χ)2= 0.17
Lower intercept: 3.4 ± 8.0 / 8.0 Ma
Y-intercept: 0.645 ± 0.031
(MSWD= 4.8)
h) him622/244 (n=70)
pooled age = 0.5 ± 0.1 Ma
central age = 0.8 ± 0.3 Ma
dispersion: 123%
p(χ2) = 0.0
Lower intercept: 6.7 ± 4.6 / 4.6 Ma
Y-intercept: 0.826 ± 0.009
(MSWD= 3.8)
standardised estimate
t/σ
207Pb/206Pb
238U/206Pb
Apatite/Chondrite
Th U La Ce Sr Sm Eu Gd Lu

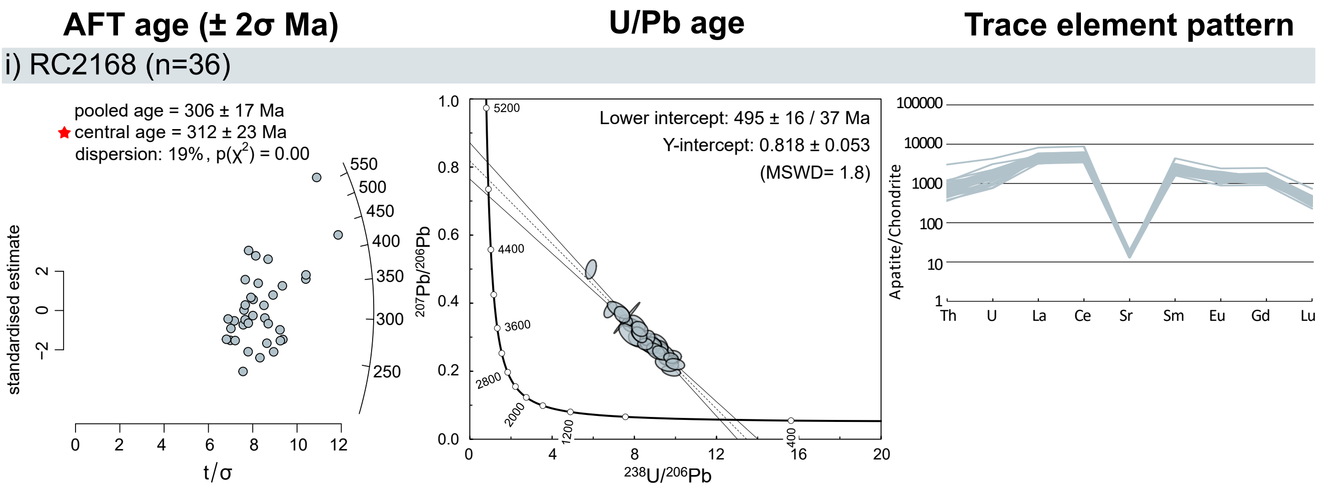
AFT age (± 2σ Ma)
U/Pb age
Trace element pattern
i) RC2168 (n=36)
pooled age = 306 ± 17 Ma
central age = 312 ± 23 Ma
dispersion: 19%, p(χ2) = 0.00
standardised estimate
t/σ
Lower intercept: 495 ± 16 / 37 Ma
Y-intercept: 0.818 ± 0.053
(MSWD= 1.8)
207Pb/206Pb
238U/206Pb
Apatite/Chondrite
Th
U
La
Ce
Sr
Sm
Eu
Gd
Lu

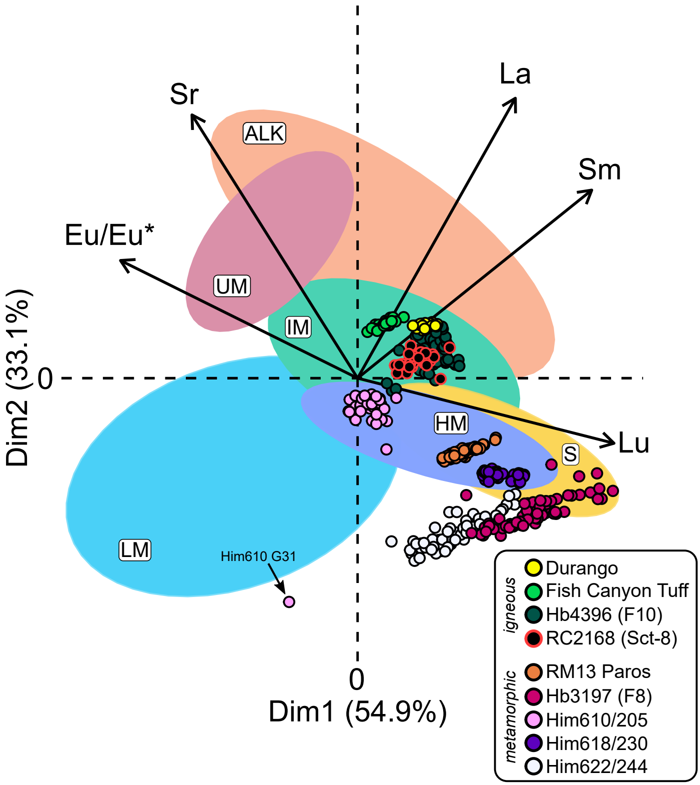

Sr
La
Sm
Eu/Eu*
Lu
ALK
UM
IM
HM
S
LM
Him610 G31
0
0
Dim2 (33.1%)
Dim1 (54.9%)
igneous
Durango
Fish Canyon Tuff
Hb4396 (F10)
RC2168 (Sct-8)
metamorphic
RM13 Paros
Hb3197 (F8)
Him610/205
Him618/230
Him622/244